Early mission radiometric performance of NOAA-21 VIIRS reflective solar bands

Ning Lei*[a], Xiaoxiong Xiong[b], Kevin Twedt[a], Amit Angal[a], Sherry Li[a], and Junqiang Sun[a]

a) Science Systems and Applications, Inc., 10210 Greenbelt Road, Lanham, MD 20706 USA;
b) Sciences and Exploration Directorate, NASA Goddard Space Flight Center, Greenbelt, MD 20771 USA
*ning.lei@ssaihq.com; phone 630-880-0071

ABSTRACT

The Visible Infrared Imaging Radiometer Suite (VIIRS) is a key instrument on the recently launched NOAA-21 (previously JPSS-2) satellite. The VIIRS, like its predecessors on the SNPP and NOAA-20 satellites, provides daily global coverage in 22 spectral bands from 0.41 to 12.0 micrometers. The geometrically and radiometrically calibrated observations are the basis for numerous operational applications and scientific research studies. Fourteen of the 22 bands are reflective solar bands (RSBs), covering wavelengths from 0.41 to 2.25 micrometers. The RSBs were radiometrically calibrated prelaunch and are regularly calibrated on orbit through the onboard solar diffuser (SD) and scheduled lunar observations. The on-orbit SD's reflectance change is determined by the onboard solar diffuser stability monitor (SDSM). Here, we report our findings on the early mission NOAA-21 VIIRS RSB radiometric performance, and the performance of the SD and the SDSM.

Index Terms: N21 VIIRS, radiometric calibration, reflective solar bands, performance, solar diffuser

1. INTRODUCTION

Following its predecessors, the Suomi National Polar-orbiting Partnership (SNPP) and NOAA-20 (N20) satellites, the NOAA-21 (N21) satellite was launched on November 10, 2022 to the same orbital plane of an equator local crossing time of 1:30 pm. One of the 4 major scientific instruments aboard N21 is the Visible Infrared Imaging Radiometer Suite (VIIRS) instrument. This is the third VIIRS instrument flying around the Earth, following the first two on SNPP and N20. With its 22 spectral bands covering wavelengths from 412 nm to 12.0 μm, VIIRS collects global top-of-the-atmosphere data with nominal spatial resolutions at nadir of 375 m and 750 m for its imaging and moderate resolution bands, respectively[1]. VIIRS data are used to produce nearly 30 biogeophysical parameters[2,3], such as sea surface temperatures, ocean color, and cloud properties. Accurate biogeophysical parameters rely on accurate radiometric calibration of the instrument.

VIIRS's 14 reflective solar bands (RSBs) have design band center wavelengths from 412 nm to 2.250 μm. Although the RSBs were calibrated prelaunch, once on orbit, the radiometric response coefficients of the detectors often change. To calibrate the detectors on orbit, VIIRS is equipped with a solar diffuser (SD), as illustrated in Fig. 1. When sunlit, the SD

provides a radiance source to calibrate the RSBs. The SD's bidirectional reflectance distribution function (BRDF) value changes over time. This change is due to solar exposure and perhaps surface contaminants. The onboard solar diffuser stability monitor (SDSM) is used to determine the change in the BRDF, with the SDSM detectors 1-7 having the same design wavelengths for the M1-7 bands and detector 8 having a design wavelength of 926 nm. This paper reports the radiometric performance of the N21 VIIRS RSBs in the early mission.

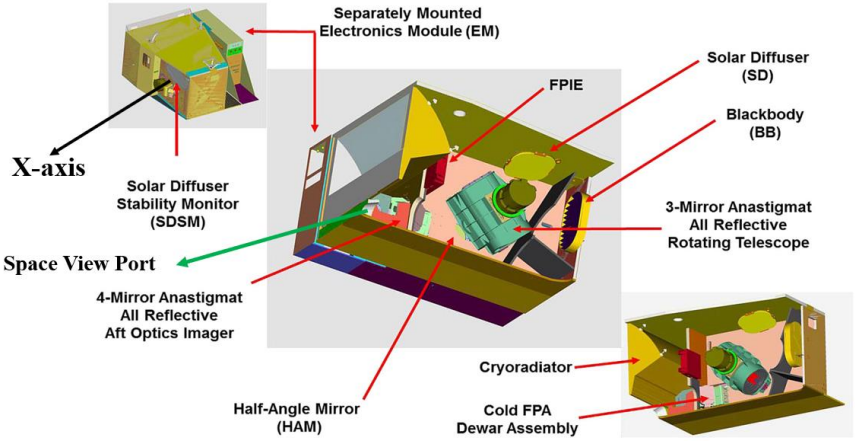

Figure 1. Relative positions of the major physical components of the VIIRS instrument.

2. RADIOMETRIC PERFORMANCE OF THE SDSM

To determine the change in the solar diffuser's BRDF, the solar diffuser stability monitor detectors compare the signal strength when looking at the Sun through the SDSM screen to the strength when looking at the sunlit SD, as illustrated by Fig. 2. Obviously, the signal-to-noise ratios (SNRs) for the SDSM detectors should be high enough so that the BRDF change can be accurately determined. The SDSM detector SNRs are affected by the detector radiometric gains, with a decreasing gain resulting in a deceasing SNR[4]. In this paper, we determine and show the SDSM detector gain change since the N21 launch.

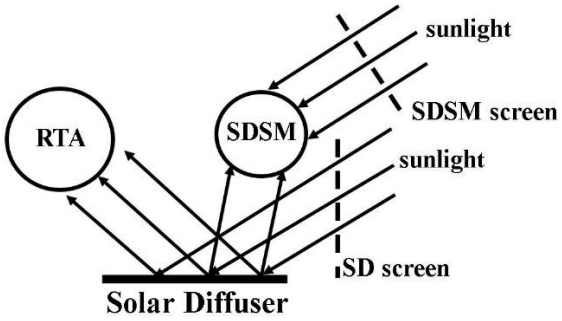

Figure 2. A schematic representation of the physical components related to the on-orbit RSB radiometric calibration of VIIRS. The RTA represents the rotating telescope assembly (the telescope) which directs incident light to the detector focal planes.

The SDSM detector gain is calculated by using the normalized detector digital count (dc) when looking at the Sun through the SDSM screen:

$$dc_{\mathrm{SUN,norm}}(t,d) = \frac{dc_{\mathrm{SUN}} d^2_{\mathrm{VIIRS-SUN}}}{\tau^{\mathrm{R}}_{\mathrm{SDSM,eff}}(\vec{\phi},d)} \quad , \tag{1}$$

where dc_{SUN} is the dark subtracted detector digital count, $d_{\mathrm{VIIRS-SUN}}$ is the distance between the VIIRS and the Sun, $\tau^{\mathrm{R}}_{\mathrm{SDSM,eff}}(\vec{\phi},d)$ is the relative effective transmittance of the SDSM screen at solar angle $\vec{\phi}$, d is the detector index, and t is time. We have shown that the ratio of $dc_{\mathrm{SUN,norm}}(t,d)$ to $dc_{\mathrm{SUN,norm}}(t=0,d)$ is the change of the measured gain for the detector[5]. The measured SDSM detector gain contains the impact of the SDSM detector relative spectral response (RSR) in a convolution sense. Because the impact of the RSRs on the gains is small, of less than 1%[5], here we use the ratio of $dc_{\mathrm{SUN,norm}}(t,d)$ to $dc_{\mathrm{SUN,norm}}(t=0,d)$ to approximate the gain's change since the launch.

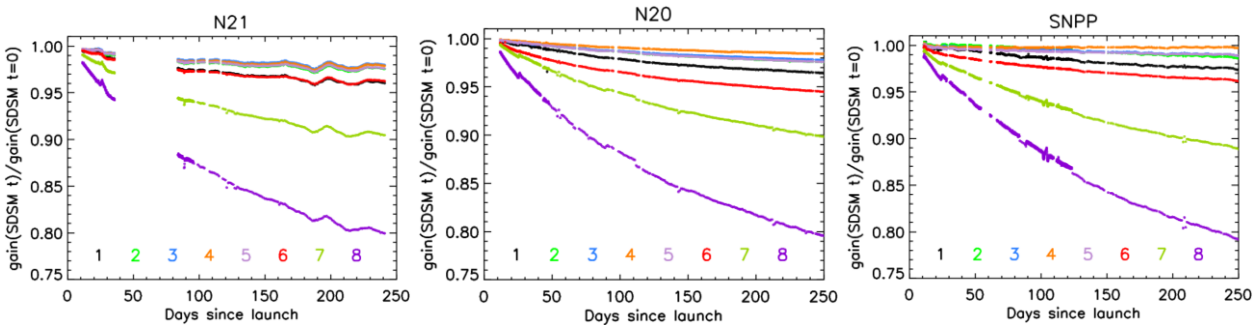

Fig. 3. (left to right) The N21, N20, and SNPP SDSM detector gain changes, normalized by the respective extrapolated values at the launch time, vs Days since launch.

The N21 VIIRS SDSM detector gains decrease in time, just as those on the SNPP and N20 VIIRS instruments. For the respective SDSM detectors on the 3 VIIRS instruments, the rates of the changes are almost the same, as shown in Fig. 3. These gain changes are thought to be from the combined impacts of the degradation of the SDSM mirror and Spherical Integrating Source's BRDF because of solar bombardment and the detector semiconductor lattice damage from solar particles[6]. As a result, the gains for the SDSM detectors 3-5 decrease with the smallest rates. The large data gap in the early days of the N21 mission, seen in the left chart in Fig. 3, is due to Ka-band transmitter 1 failure. The redundant Ka-band transmitter 2 started to operate on February 2, 2023.

3. RADIOMETRIC PERFORMANCE OF THE SOLAR DIFFUSER

The SD's BRDF change, known as the H-factor[1], is determined by the SDSM through the ratio of the signal strengths when looking at the Sun and the SD:

$$H^{\mathrm{mea}}_{\mathrm{SDSM}}(\lambda_d, t, \vec{\phi}(t)) = \frac{S_{\mathrm{H}} \times \frac{dc_{\mathrm{SD}}(t,d)}{dc_{\mathrm{SUN}}(t',d)} \times \frac{\tau^{\mathrm{R}}_{\mathrm{SDSM,eff}}(\vec{\phi}(t'),d)}{\tau^{\mathrm{R}}_{\mathrm{SD,eff}}(\vec{\phi}(t),d)}}{\mathrm{BRDF}_{\mathrm{SDSM}}\left(\lambda_d, 0, \vec{\phi}(t)\right) \sin\phi_{\mathrm{V,SD}}(t)}, \tag{2}$$

where λ_d denotes the SDSM detector center wavelength, dc_{SD} is the detector digital count when viewing the sunlit SD, $\tau^{\mathrm{R}}_{\mathrm{SD,eff}}$ is the relative effective SD screen transmittance, t and t' are the times for the data collection at the SD and Sun views, respectively, and $\phi_{\mathrm{V,SD}}$ is the angle between the solar vector and the SD surface (note: 90° - $\phi_{\mathrm{V,SD}}$ is the solar incident angle with respect to the SD surface). In Eq. (2), S_{H} is a scale factor in units of 1/steradians, determined by the condition: $H^{\mathrm{mea}}_{\mathrm{SDSM}}\left(\lambda_d, t, \vec{\phi}(t=0)\right) = 1$. Note that because t and t' are very close, separated by the telescope scan duration of about 1.8 seconds, the SDSM detector gains at the SD and Sun views are essentially the same and cancelled in Eq. (2). A further note is that $H^{\mathrm{mea}}_{\mathrm{SDSM}}$ is the directly measured H-factor for the SDSM SD view. This H-factor is the true H-factor

for the same view convolved with the SDSM RSR and the solar spectral power[5]. The SDSM screen transmittance and the product of the SD screen transmittance and the BRDF at the launch time are improved upon the prelaunch values[7], by using the calibration data collected at the yaw maneuver orbits of 1649 to 1663.

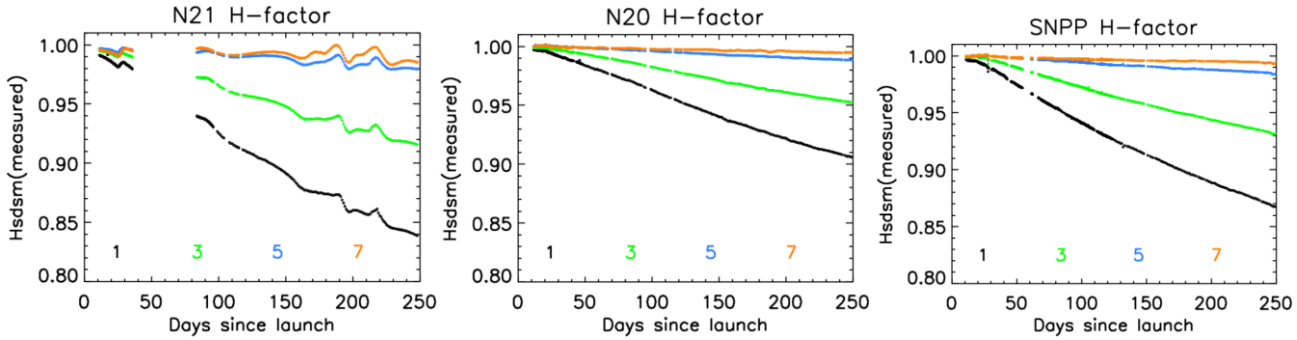

Fig. 4. (Left to right) N21, N20, and SNPP VIIRS SD H-factors measured by the respective onboard SDSMs vs Days since launch for the SDSM detectors 1 (black), 3 (green), 5 (cyan), and 7 (orange).

Just as the SD BRDF H-factors for the SNPP and N20 VIIRS, the N21 VIIRS SD H-factor, in general, decreases with time, with the largest degradation at the shortest wavelength, as shown in left chart in Fig. 4. For comparison, in Fig. 4 we also show the measured H-factors for the SNPP and N20 VIIRS. Among the three VIIRS instruments, the measured H-factor for the N21 VIIRS decreases the most at the respective wavelengths, as illustrated in Fig. 4. Because of the angular dependence, the H-factors shown in Fig. 4 are for the angle between the solar vector and the SD surface at 35.5°. The large undulations seen for the N21 VIIRS H-factors are due to the inaccuracy in the SDSM screen function. The inaccuracy also causes the large undulations seen for the SDSM detector gains, as shown in left chart in Fig. 3. As we did before for the SNPP and N20 VIIRS[8], once we have enough regular on-orbit calibration data that cover the solar angles over the mission, we will update the screen functions again, using the calibration data collected at both the regular times and on the yaw maneuver orbits. We expect the refined screen functions will result in much smoother SDSM detector gain and H-factor versus time curves.

4. RADIOMETRIC PERFORMANCE OF THE RSB

The Earth scene spectral radiance is calculated by

$$L_{EV} = F \times (c_0 + c_1 dn_{EV} + c_2 dn_{EV}^2 + c_3 dn_{EV}^3)/RVS(\lambda_B, \theta_{EV}) \quad , \tag{3}$$

where the c-coefficients are interpolated (in focal plane and electronics temperatures) prelaunch values, dn_{EV} is the dark-subtracted Earth view detector digital number, λ_B is the band center wavelength, θ_{EV} is the solar incident angle with respect to the half-angle-mirror (HAM) when the telescope views the Earth, and RVS is the HAM's reflectivity relative to that when the telescope views the SV. Currently, c_0 and c_3 are set to be zero for all RSB detectors. The dark digital number is collected when the detector views the Space View (SV) port which provides a deep space scene. The F in Eq. (3), known as the F-factor, is a correction factor so that the right side of Eq. (3) can yield a correct scene spectral radiance. The on-orbit change in the F-factor is an important aspect of the detector's radiometric performance.

The F-factor is obtained by using the dn collected when the detector views the onboard solar diffuser (SD) during the time when the SD is fully solar illuminated through the SD screen. Mathematically, the F-factor is calculated by

$$F = \frac{L_{SD} RVS(\lambda_B, \theta_{SD})}{c_0 + c_1 dn_{SD} + c_2 dn_{SD}^2 + c_3 dn_{SD}^3} \quad , \tag{4}$$

where θ_{SD} is the solar incident angle with respect to the HAM when the telescope views the SD and dn_{SD} is the dark-subtracted detector digital number when viewing the sunlit SD. In Eq. (4), L_{SD} is the spectral radiance provided by the sunlit SD, calculated by

$$L_{SD} = \frac{\int_0^\infty RSR \times d\lambda \times \frac{\Phi_{\mathrm{SUN}}(\lambda,t)}{4\pi d^2_{\mathrm{VIIRS-SUN}}} \times \tau_{\mathrm{SD}} \mathrm{BRDF}_{\mathrm{RTA}}(\lambda,0,\vec{\phi}) H_{\mathrm{RTA}}(\lambda,t,\vec{\phi}) \sin\phi_{\mathrm{V,SD}}}{\int_0^\infty RSR \times d\lambda}, \quad (5)$$

where the RSR is the relative spectral response for the RSB detector, Φ_{SUN} is the solar spectral power, $\tau_{\mathrm{SD}}\mathrm{BRDF}_{\mathrm{RTA}}(\lambda,0,\vec{\phi})$ is the product of the SD screen transmittance and the SD's BRDF at the launch time, improved from the calibration data collected at the yaw maneuver orbits and scaled to match the prelaunch $\tau_{\mathrm{SD}}\mathrm{BRDF}_{\mathrm{RTA}}(\lambda,0,\vec{\phi})$ over the solar angles, and λ is the solar photon wavelength. In Eq. (5), $H_{\mathrm{RTA}}(\lambda,t,\vec{\phi})$ is the change in the SD's BRDF since the launch for the telescope SD view.

We can find $H_{\mathrm{RTA}}(\lambda,t,\vec{\phi})$ through multi-year lunar observations as we did for the SNPP VIIRS[5]. We also used the SNPP VIIRS results for the $\mathrm{H_{RTA}}$ model to find the N20 VIIRS $H_{\mathrm{RTA}}(\lambda,t,\vec{\phi})$ by comparing the H-factor solar angular dependence strengths for the two sensors[4]. Here, we find the N21 VIIRS SD H_{RTA} by using the average of the ratios of $H_{\mathrm{RTA}}/H^{\mathrm{mea}}_{\mathrm{SDSM}}$ for the previous two VIIRS instruments:

$$H_{\mathrm{RTA}}(\lambda,t,\vec{\phi};N21) = H^{\mathrm{mea}}_{\mathrm{SDSM}}(N21) * \frac{\frac{H_{\mathrm{RTA}}(SNPP)}{H^{\mathrm{mea}}_{\mathrm{SDSM}}(SNPP)} + \frac{H_{\mathrm{RTA}}(N20)}{H^{\mathrm{mea}}_{\mathrm{SDSM}}(N20)}}{2}. \quad (6)$$

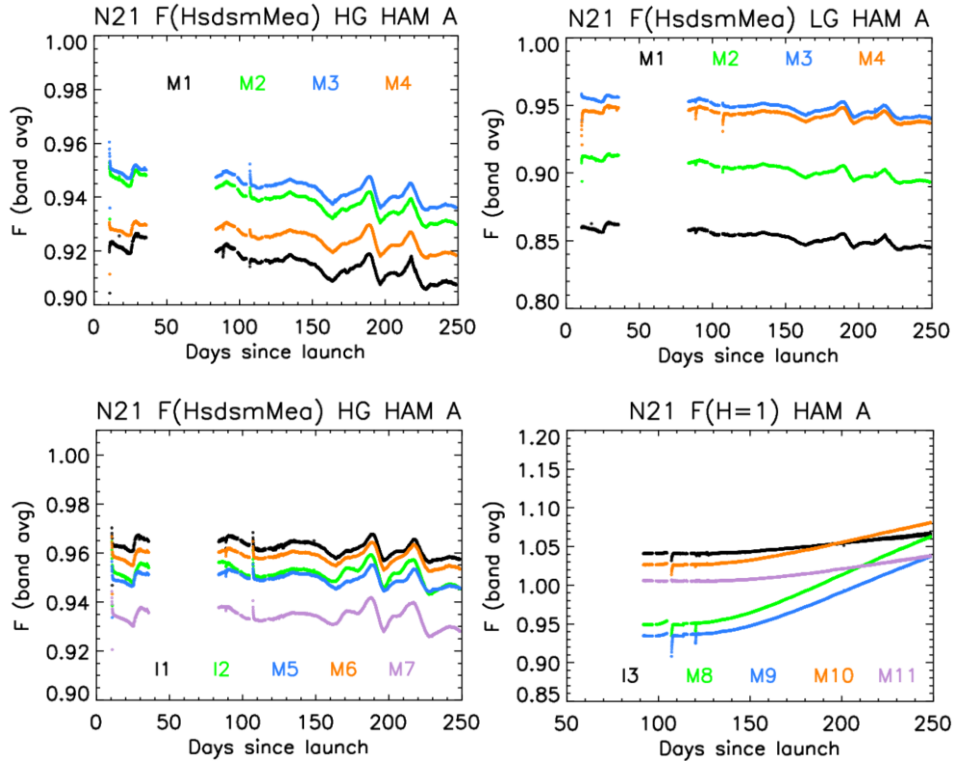

Fig. 5. (Top) The N21 VIIRS F-factors vs days since launch for the M1-M4 bands, averaged over the detectors in each band, calculated with the SDSM measured H-factors, at the high-gain (top left) and low-gain (top right) stages, and HAM side A. (Bottom) The N21 VIIRS F-factors vs days since launch for the I1-I3 and M5-M11 bands, averaged over the detectors in each band, calculated with the SDSM measured H-factors for the I1-I2, M5-M7 bands and H=1 for the SWIR bands, at HAM side A, and the high-gain stages for the dual-gain bands.

If the F-factor is correctly calculated with correct inputs, including correct c-coefficients, then the F-factor should be 1. The F-factors calculated from Eq. (4) are close to one, as shown in Fig. 5. We believe the deviation from one mainly comes from the inaccuracy in c_1 because the prelaunch calibration source has a larger error requirement of 5%. Errors in $\tau_{\mathrm{SD}}\mathrm{BRDF}_{\mathrm{RTA}}(\lambda, 0, \vec{\phi})$ also contribute to the difference.

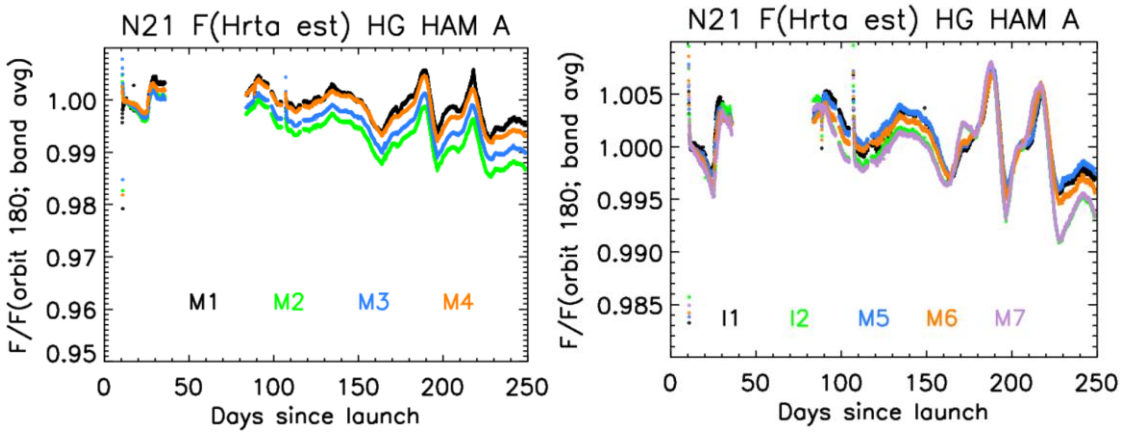

Fig. 6. The N21 VIIRS VISNIR band F-factors vs days since the satellite launch, normalized to their respective values at orbit 180 and averaged over the detectors in each VISNIR band, at HAM side A and high-gain stage for dual-gain bands.

The F-factors for the VISNIR bands, after being averaged over the detectors in each band, trend slightly downwards in time, as shown in Fig. 6. These downward trends may reflect the fact that our calculation of the BRDF on-orbit change factor, the H-factor, by using Eq. (6), may not be accurate enough. We are considering using our previous approach to find H_{RTA} for the N21 VIIRS by using the SNPP and/or N20 VIIRS results[4].

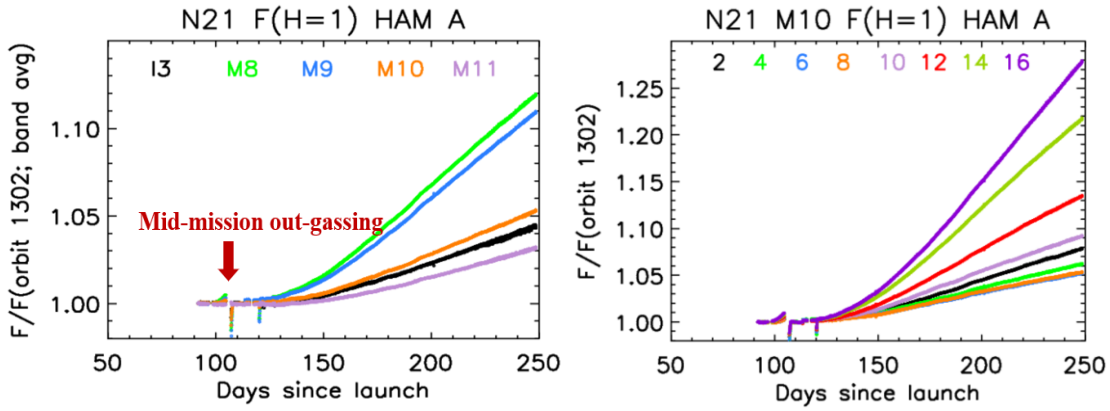

Fig. 7. (Left) The N21 VIIRS SWIR band F-factors (calculated with H_{RTA}=1) vs days since the satellite launch, normalized to their respective values at orbit 1302 and averaged over the detectors in each SWIR band. (Right) The N21 VIIRS band M10 F-factors (calculated with H_{RTA}=1) for the even indexed detectors, normalized to the respective values at orbit 1302.

The N21 SWIR bands become usable since satellite orbit 1302 (Feb. 10, 2023) when the focal plane temperature stabilized first to 82 K and shortly afterwards to 80 K. The F-factors for the SWIR bands are calculated with H_{RTA}=1. The F-factors, in general, trend upwards, as shown in Fig. 7, indicating degradation of the radiometric gains. To restore the radiometric performance for the SWIR bands, a mid-mission outgassing was performed on February 23-24, 2023. Right after the mid-mission outgassing, the F-factors returned to the respective at-launch values, just as the case for the N20 VIIRS SWIR bands. But soon after that the SWIR band radiometric gains started to degrade again, by the largest amount for the M8 band and the smallest for the M11 band. The degradation is detector index dependent, as shown in the right chart in Fig. 7. The approximation of H_{RTA}=1 for the N21 VIIRS SWIR bands in the early mission is justified. For the SNPP VIIRS,

H_{RTA} changed less than 0.2% at the M8 band center wavelength at the end of the first year in the mission[9]. (The H_{RTA} changes much less for the N20 VIIRS at the same wavelength.) Note that band M11 prelaunch $\tau_{SD}BRDF_{RTA}(\lambda, 0, \vec{\phi})$ is multiplied by 1.061 so that the observed lunar irradiances[10] for the N20 and N21 VIIRS band M11 agree. This adjustment is justified by the fact that the prelaunch $\tau_{SD}BRDF_{RTA}$ was measured in wavelength up to that for band M10 (1.61 μm). Band M11 (2.25 μm) prelaunch $\tau_{SD}BRDF_{RTA}$ is obtained from an extrapolation. Because the much larger uncertainty associated with the N21 VIIRS prelaunch $\tau_{SD}BRDF_{RTA}$, the extrapolation can result in a much larger error.

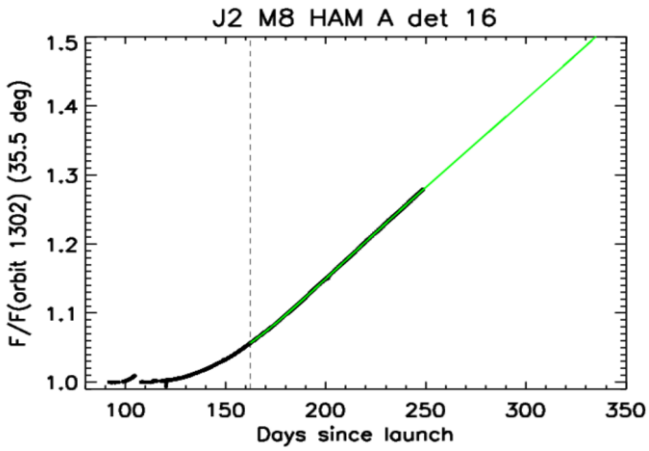

Fig. 8. Black dots are for the measured F-factors divided by its value at orbit 1302 when the SMWIR band focal plane temperature first stabilized, for the N21 M8 detector 16 HAM side A. The solid green line is from Eq. (7) to the measured normalized F-factors after the vertical dashed line.

To reduce the frequency of the forward F-factor Look-Up-Table delivery for the NASA N21 VIIRS Level-1B Earth reflectance products, we use a physical model to predict future SWIR band F-factors:

$$\frac{F(t)}{F(t0)} = \exp\{a0 + |a1|(t - t0) * [1 + |a2|(t - t0) * \exp(-|a3| * (t - t0))]\}. \quad (7)$$

The model assumes that a layer of material absorbs light, with the layer thickness changing with a changing speed. The acceleration of the speed decreases exponentially. An example to apply Eq. (7) is for the M8 detector 16, as shown in Fig. 8. In performing the fit, we use measured F-factors from orbits 2300 to 3428 (set t0=orbit 2300). Although the model performs well, as shown by the good agreement between the measured (black dots) and the modeled (solid green line) F-factors, it remains to be seen whether this model can adequately address the changes in the SWIR band gains over larger time durations.

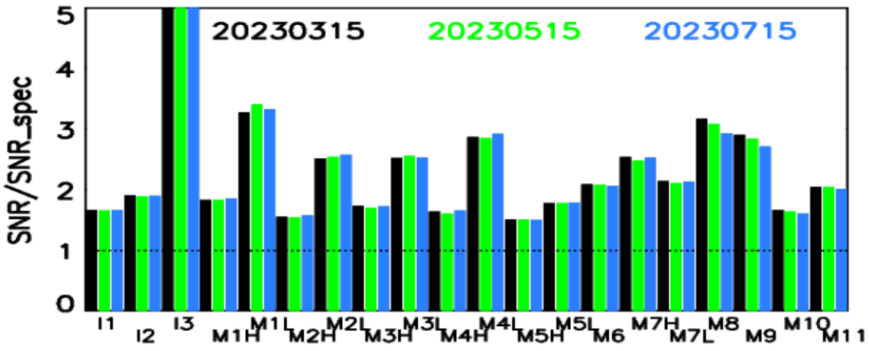

Fig. 9. Ratios of the measured SNRs at the respective Ltyp to the specifications for the N21 VIIRS RSBs at 20230315 (black), 20230515 (green) and 20230715 (cyan).

The SNRs at the respective Ltyp for all the N21 VIIRS RSB detectors are calculated by using the same approach as that for the previous VIIRS instruments[11]. The SNRs are all above the respective required values with margins. Fig. 9 shows the ratios of the measured SNRs to the respective requirements, averaged across the detectors in a band. The SNRs for the SWIR bands decrease in time, as expected, because of the decreasing gains (increasing F-factors) with an increasing time.

5. SUMMARY

The N21 VIIRS reflective solar bands have been radiometrically calibrated by using the onboard sunlit SD since the focal plane temperatures were stabilized. To calibrate the VISNIR bands, we use the onboard SDSM to determine the SD's BRDF on-orbit change factor, the H-factor. However, the SDSM directly measured H-factor, $H_{\mathrm{SDSM}}^{\mathrm{mea}}$, is not for the telescope SD view. To approximate the H-factor for the telescope SD view, H_{RTA}, we multiply $H_{\mathrm{SDSM}}^{\mathrm{mea}}$ by a factor that is the average of $H_{\mathrm{RTA}}/H_{\mathrm{SDSM}}^{\mathrm{mea}}$ for the SNPP and N20 VIIRS. The VISNIR band F-factors trend downwards slightly in time. To calibrate the SWIR bands, we use H_{RTA}=1. The SWIR band F-factors trend upwards in time, the most for the M8 band (1.61 μm) and the least for the M11 band (2.25 μm). Right after the mid-mission out-gassing, the SWIR band F-factors returned to their respective original values, but soon after that the F-factors started to trend up in time again. The changes in the F-factors result in the movements of the respective SNRs. For the VISNIR bands, the F-factors are nearly constants in time, and so the SNRs. For the SWIR bands, the SNRs trend downwards in time, just as the detector gains (1/F-factors). Nevertheless, all the SNRs are above the requirements with margins. For a given SDSM detector, the N21 VIIRS $H_{\mathrm{SDSM}}^{\mathrm{mea}}$ decreases in time, with a rate slightly larger than that for the SNPP VIIRS whereas the N21 VIIRS SDSM detector gains decrease in time, mostly the same as those for the SNPP and N20 VIIRS.

REFERENCES

[1] Joint Polar Satellite System (JPSS) VIIRS Radiometric Calibration Algorithm Theoretical Basis Document (ATBD); NASA Goddard Space Flight Center: Greenbelt, MD, USA, 2013.

[2] Zhou, L., Divakarla, M., Liu, X., Layns, A., Goldberg, M, "An Overview of the Science Performances and Calibration/Validation of Joint Polar Satellite System Operational Products", Remote Sens. **11**, 698, (2019).

[3] Cao, C., De Luccia, F. J., Xiong, X., Wolfe, R., Weng, F., "Early On-Orbit Performance of the Visible Infrared Imaging Radiometer Suite Onboard the Suomi National Polar-Orbiting Partnership(S-NPP) Satellite", IEEE Trans. Geosci. Remote Sens. **52**(2), 1142-1156 (2013).

[4] Lei, N., Twedt, K., Xiong, X., Angal, A., "Performance of NOAA-20 VIIRS Solar Diffuser and Solar Diffuser Stability Monitor", IEEE Trans. Geosci. Remote Sens. **59**(9), 7180-7188 (2021); doi: 10.1109/TGRS.2020.3032068.

[5] Lei, N., Xiong, X., Wang, Z., Li, S., Twedt, K., "SNPP VIIRS RSB on-orbit radiometric calibration algorithms Version 2.0 and the performances, part 1: the algorithms," J. Appl. Remote Sens. **14**(4), 047501 (2020); doi: 10.1117/1.JRS.14.047501.

[6] De Luccia, F., Moyer, D., Johnson, E., Rausch, K., Lei, N., Chiang, K., Xiong, X., Fulbright, J., Hass, E., and Iona, G., "Discovery and characterization of on-orbit degradation of the Visible Infrared Imaging Radiometer Suite (VIIRS) Rotating Telescope Assembly (RTA)", Proc. SPIE **8510**, Art ID: 8510-1A (2012).

[7] Sun, J., Chu, M., and Wang, M., "On-orbit characterization of the VIIRS solar diffuser and attenuation screens for NOAA-20 using yaw measurements", Appl. Optics **57**(22), 6605-6619 (2018).

[8] Lei, N., Chen, X., and Xiong, X., "Determination of the SNPP VIIRS SDSM Screen Relative Transmittance from Both Yaw Maneuver and Regular On-Orbit Data", IEEE Trans. Geosci. Remote Sens. **54**, 1390-1398 (2016); doi: 10.1109/TGRS.2015.2480039.

[9] Lei, N., Xiong, X., Wang, Z., Li, S., Twedt, K., "SNPP VIIRS RSB on-orbit radiometric calibration algorithms Version 2.0 and the performances, part 2: the performances," J. Appl. Remote Sens. **14**(4), 047502 (2020); doi: 10.1117/1.JRS.14.047502.

[10] Xiong, X., Sun, J., Fulbright, J., Wang, Z., and Butler, J., "Lunar Calibration and Performance for S-NPP VIIRS Reflective Solar Bands," IEEE Trans. Geosci. Remote Sens., **54** (2), 1052-1061 (2016).

[11] Twedt, K., Lei, N., Xiong, X., Angal, A., Li, S., Chang, T., and Sun, J., "On-Orbit Calibration and Performance of NOAA-20 VIIRS Reflective Solar Bands", IEEE Trans. Geosci. Remote Sens. **60**, art-ID: 1001413 (2022); doi: 10.1109/TGRS.2021.3108970.